Linear-Nonlinear Cascades Capture Synaptic Dynamics

Julian Rossbroich[1◑], Daniel Trotter[2◑], John Beninger [3], Katalin Tóth[3], Richard Naud[2,3*]

1 Friedrich Miescher Institute for Biomedical Research, Basel, Switzerland
2 Department of Physics, University of Ottawa, Ottawa, ON, Canada
3 uOttawa Brain Mind Institute, Center for Neural Dynamics, Department of Cellular and Molecular Medicine, University of Ottawa, Ottawa, ON, Canada

◑These authors contributed equally to this work.
* rnaud@uottawa.ca

Abstract

Short-term synaptic dynamics differ markedly across connections and strongly regulate how action potentials communicate information. To model the range of synaptic dynamics observed in experiments, we have developed a flexible mathematical framework based on a linear-nonlinear operation. This model can capture various experimentally observed features of synaptic dynamics and different types of heteroskedasticity. Despite its conceptual simplicity, we show that it is more adaptable than previous models. Combined with a standard maximum likelihood approach, synaptic dynamics can be accurately and efficiently characterized using naturalistic stimulation patterns. These results make explicit that synaptic processing bears algorithmic similarities with information processing in convolutional neural networks.

Author summary

Understanding how information is transmitted relies heavily on knowledge of the underlying regulatory synaptic dynamics. Existing computational models for capturing such dynamics are often either very complex or too restrictive. As a result, effectively capturing the different types of dynamics observed experimentally remains a challenging problem. Here, we propose a mathematically flexible linear-nonlinear model that is capable of efficiently characterizing synaptic dynamics. We demonstrate the ability of this model to capture different features of experimentally observed data.

Introduction

The nervous system has evolved a communication system largely based on temporal sequences of action potentials. A central feature of this communication is that action potentials are communicated with variable efficacy on short (10 ms - 10 s) time scales [1–6]. The dynamics of synaptic efficacy at short time scales, or short-term plasticity (STP), can be a powerful determinant of the flow of information, allowing the same axon to communicate independent messages to different post-synaptic targets [7, 8]. Properties of STP vary markedly across projections [9–11], leading to the idea that connections belong to distinct classes [12, 13] and that these distinct classes shape information transmission in vivo [14–16]. Thus, to understand the flow of

information in neuronal networks, structural connectivity must be indexed with an accurate description of STP properties.

One approach to characterizing synaptic dynamics is to perform targeted experiments and extract a number of summary features. The most common feature extracted is the paired-pulse ratio [5, 17–19], which is inferred by presenting two stimulations and taking the ratio of the response to the second stimulation over the response to the first. This ratio can be used to classify a synapse as short-term depressing (STD) or short-term facilitating (STF). In addition, longer and more complex stimulation patterns suggest a variety of STP types, such as delayed facilitation onset [6], biphasic STP [20, 21] and distinct supra- and sub-linear facilitation [22]. However, without a model it is difficult to understand which observations are consistent with each other, and which come as a surprise. If it is both accurate and flexible, a model can 'compress' the data into a small number components.

Previous efforts have fit a mechanistic mathematical model using all available experimental data, with parameters that correspond to physical properties [23]. In this vein, the model proposed by Tsodyks and Markram captures the antagonism between transient increases in vesicle release probability and transient depletion of the readily releasable vesicle pool [11, 24, 25]. Optimizing parameter values to best fit the observed data provides an estimate of biophysical properties [26, 27]. This simple model is highly interpretable, but its simplicity restricts its ability to capture the diversity of synaptic responses to complex stimulation patterns. Complex STP dynamics rely on interactions between multiple synaptic mechanisms that cannot be described in a simplified framework of release probability and depletion. To describe the dynamics of complex synapses, the Tsodyks-Markram model therefore requires multiple extensions [23, 28], such as, vesicle priming, calcium receptor localization, multiple timescales, or use-dependent replenishment [6, 29–31]. As a compendium of biophysical properties is collected, these properties become increasingly difficult to adequately characterize based on experimental data because degeneracies and over-parametrization lead to inefficient and non-unique characterization. Taken together, current approaches appear to be either too complex for accurate characterization, or insufficient to capture all experimental data.

The trade-off between a model's interpretability and its ability to espouse complex experimental data echoes similar trade-offs in other fields, such as in the characterization of the input-output function of neurons [32–37]. Taking a systems identification approach, we chose to sacrifice some of our model's interpretability in order to avoid over-parametrization and degeneracies while still capturing the large range of synaptic capabilities. Inspired by the success of linear-nonlinear models for the characterization of cellular responses [32, 33], we extended previous phenomenological approaches to synaptic response properties [3, 4, 38, 39] to account for nonlinearities and kinetics evolving on multiple time scales. The resulting Spike Response Plasticity (SRP) model captures short-term facilitation, short-term depression, biphasic plasticity, as well as sub- and supra-linear facilitation and post-burst potentiation. Using standard gradient descent algorithms, model parameters can be inferred accurately with limited amounts of experimental data. Because it combines a layer of convolution with a nonlinear readout, our modelling framework has striking parallels with deep convolutional neural networks. That is, our framework suggests that synaptic dynamics can be conceptualized as extending information processing that occurs via dendritic integration, which constitutes a contribution to information processing theory for synapses.

Results

Deterministic Dynamics

To construct our statistical framework, we first considered the deterministic dynamics of synaptic transmission. Our goal was to describe the dynamics of the amplitude of individual post-synaptic currents (PSCs). Specifically, a presynaptic spike train will give rise to a post-synaptic current trace, $I(t)$, made of a sum of PSCs triggered by presynaptic action potentials at times t_j:

$$I(t) = \sum_j \mu_j k_{PSC}(t - t_j), \tag{1}$$

where k_{PSC} is the stereotypical PSC time course and μ_j is the synaptic efficacy, or relative amplitude, of the jth spike in the train normalized to the first spike in the train ($\mu_1 = 1$).

To begin modeling synaptic dynamics, we sought a compact description for generating $I(t)$ from the presynaptic spike train, $S(t)$. Spike trains are mathematically described by a sum of Dirac delta-functions, $S(t) = \sum_j \delta(t - t_j)$ [35]. For our purposes, we assumed the time course of individual PSCs to remain invariant through the train, but PSC amplitude is dynamic. To capture these amplitude changes, we introduce the concept of an efficacy train, $E(t)$, made of a weighted sum of Dirac delta-functions: $E(t) = \sum_j \mu_j \delta(t - t_j)$. The efficacy train can be conceived as a multiplication between the spike train and a time-dependent signal, $\mu(t)$, setting the synaptic efficacy at each moment of time

$$E(t) = \mu(t)S(t). \tag{2}$$

Thus the current trace can be written as a convolution of the efficacy train and the stereotypical PSC shape, $\mathbf{k}_{PSC}$: $I = \mathbf{k}_{PSC} * E$, where $*$ denotes a convolution. In this way, because in typical electrophysiological assays of synaptic properties the PSC shape ($\mathbf{k}_{PSC}$) is known and the input spike train $S(t)$ is controlled, characterization of synaptic dynamics boils down to a characterization of how the synaptic efficacies evolve in response to presynaptic spikes. Mathematically, we sought to identify the function $\mu[S(t)]$ of the spike train $S(t)$.

Using this formalism, we aim to build a general framework for capturing synaptic efficacy dynamics. Previous modeling approaches of STP have used a system of nonlinear ordinary differential equations to capture $\mu(t)$ separated in a number of dynamic factors [4, 11, 23, 24]. Our main result is that we propose a linear-nonlinear approach inspired from the engineering of systems identification [33, 40–47] and the Spike Response Model (SRM) for cellular dynamics [34, 48, 49]. Here, the efficacies are modeled as a nonlinear readout, f, of a linear filtering operation:

$$\mu = \frac{1}{f(b)} f\left(\mathbf{k}_\mu * S + b\right) \tag{3}$$

where $\mathbf{k}_\mu(t)$ is the *efficacy kernel* describing the spike-triggered change in synaptic efficacy and b is a baseline parameter, which could be absorbed in the definition of the efficacy kernel. The efficacy kernel can be parametrized by a linear combination of nonlinear basis functions (see Methods). Importantly, although $\mathbf{k}_\mu$ can be formalized as a sum of exponentially decaying functions, the choice of basis functions does not force a specific timescale onto the efficacy kernel. Instead, it is the relative weighting of different timescales that will be used to capture the effective timescales. In this way, while $\mathbf{k}_{PSC}$ regulates the stereotypical time-course of a single PSC, the efficacy kernel, $\mathbf{k}_\mu$, regulates the stereotypical changes in synaptic efficacy following a pre-synaptic action potential. The efficacy kernel can take any strictly causal form ($k_\mu(t) = 0$ for

$t \in -\infty, 0]$), such that a spike at time t_j affects neither the efficacy before nor at time t_j, but only after t_j. Here we call the 'potential efficacy' the result of the convolution and baseline, $\mathbf{k}_\mu * S + b$, before taking a sigmoidal nonlinear readout. Although some early studies have used a linear readout [4], synaptic dynamics invoke mechanisms with intrinsic nonlinearities, like the saturation of release probability or the fact that the number of vesicles cannot be negative. The readout, $f(\cdot)$, will capture the nonlinear progression of PSC amplitudes in response to periodic stimulation. The factor $f(b)^{-1}$ was introduced because we consider the amplitudes normalized to the first pulse, replaceable by an additional parameter when treating non-normalized amplitudes. This version of the deterministic SRP model, can capture different types of STP by changing the shape of the efficacy kernel.

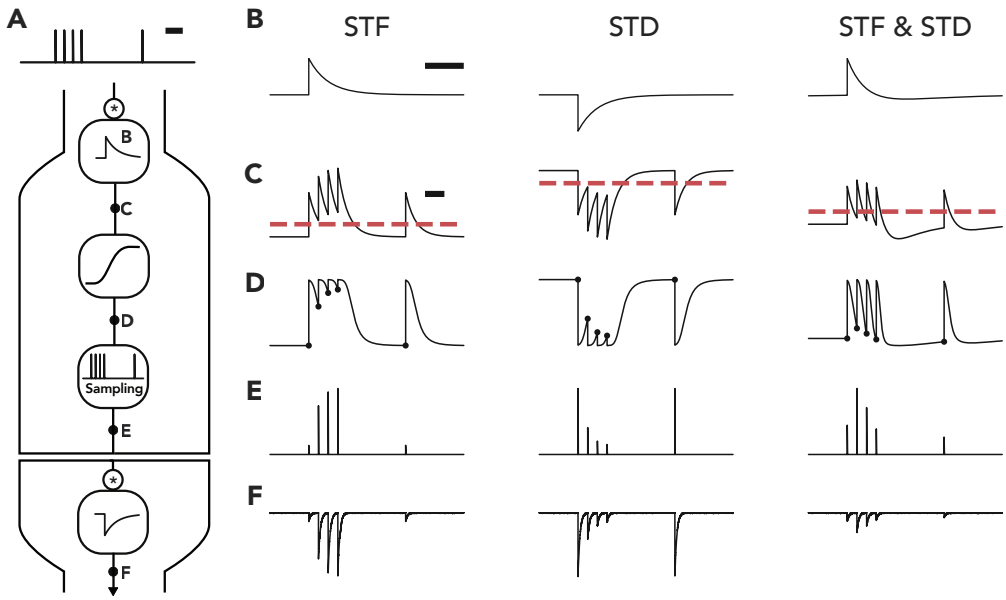

Fig 1. The SRP model captures different types of short-term plasticity. **A** The model first passes a pre-synaptic spike train through a convolution with the efficacy kernel. We illustrate three choices of this efficacy kernel: (**B**), a positive kernel for STF (left), a negative kernel for STD (middle) and one for STF followed by STD (right). After the convolution and combination with a baseline (**C**; dashed line indicates zero), a nonlinear readout is applied, leading to the time-dependent efficacy $\mu(t)$ (**D**). This time-dependent signal is then sampled at the spike times, leading to the efficacy train (**E**) and thus to the post-synaptic current trace (**F**). Scale bars correspond to 100 ms.

Short-Term Facilitation and Depression

To show that the essential phenomenology of both STF and STD can be encapsulated by an efficacy kernel $\mathbf{k}_\mu$, we studied the response to a burst of four action potentials followed by a delay and then a single spike and compared responses obtained when changing the shape of the efficacy kernel (Fig. 1A). For simplicity, we considered $\mathbf{k}_\mu$ to be a mono-exponential decay starting at time 0. When the amplitude of this filter is positive (Fig. 1B, left), a succession of spikes leads to an accumulation of potential efficacy ($\mathbf{k}_\mu * S + b$, Fig. 1C, left). After the sigmoidal readout (Fig. 1D, left) and sampling at the spike times, the efficacy train (Fig. 1E, left) and the associated current

trace (Fig. 1F, left) showed facilitation. Choosing a negative amplitude (Fig. 1B, middle) gave rise to the opposite phenomenon. In this case, the succession of spikes gradually decreased potential efficacy ($\mathbf{k}_\mu * S + b$, Fig. 1C, middle). Following the sigmoidal readout (Fig. 1D, middle) the efficacy train (Fig. 1E, middle) and the resulting current trace (Fig. 1F, middle) showed STD dynamics. Conveniently, changing the polarity of the efficacy kernel controls whether synaptic dynamics follow STF or STD.

At many synapses, facilitation apparent at the onset of a stimulus train is followed by depression, a phenomenon referred to as biphasic plasticity [20, 21, 50]. To model this biphasic plasticity in our framework, we considered an efficacy kernel consisting of a combination of two exponential-decays with different decay timescales and opposing polarities. By choosing the fast component to have a positive amplitude and the slow component to have a negative amplitude (Fig. 1B, right), we obtained a mixture between the kernel for STF and the kernel for STD. Under these conditions, a succession of spikes creates an accumulation of potential efficacy followed by a depreciation ($\mathbf{k}_\mu * S + b$, Fig. 1C, right). Once the sigmoidal readout was performed (Fig. 1D, right), the efficacy train (Fig. 1E, right) and the resulting PSC trace (Fig. 1F, right) showed facilitation followed by depression. Thus, the model captured various types of STP by reflecting the facilitation and depression in positive and negative components of the efficacy kernel, respectively.

Sublinear and Supralinear Facilitation

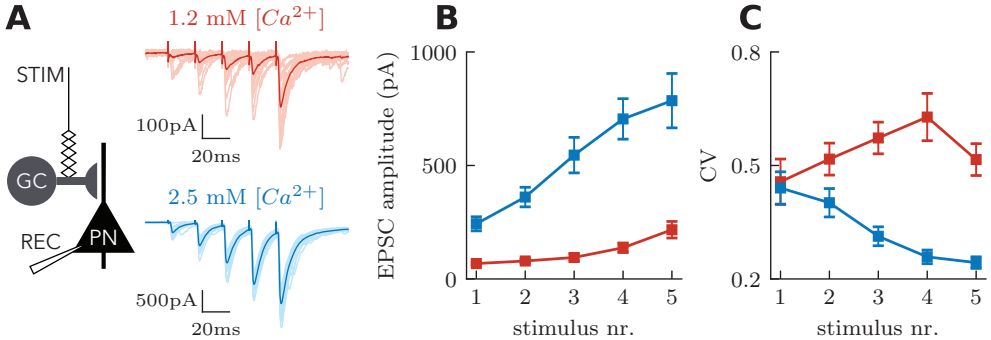

Fig 2. Effects of extracellular calcium concentration on STP dynamics at hippocampal mossy fiber synapses. **A** Mossy fiber short-term facilitation in 1.2 mM (red) and 2.5 mM (blue) extracellular [Ca^{2+}]. EPSCs recorded from CA3 pyramidal cells in response to stimulation of presynaptic mossy fibers (50 Hz, 5 stimuli). **B** EPSC peak amplitudes as a function of stimulus number. The time course of facilitation varies dependent on the initial release probability. **C** The coefficient of variation (CV), measured as the standard deviation of EPSCs divided by the mean, is increased in 1.2 mM extracellular [Ca^{2+}]. Data redrawn from [22].

The typical patterns of facilitation and depression shown in Fig. 1 are well captured by the traditional Tsodyks-Markram (TM) model [24–26]. This model captures the nonlinear interaction between depleting the readily releasable pool of vesicles (state variable R) and the probability of release (state variable u; see Methods for model description). We, therefore, asked whether our modeling framework could capture experimentally observed features that require a modification of the classical TM model. While previous work has extended the TM model for use-dependent depression [29] and receptor desensitization [23], we considered the nonlinear facilitation observed in mossy fiber synapses onto pyramidal neurons (MF-PN) in response to a burst of action

potentials (Fig. 2A). In these experiments, the increase of PSC amplitudes during the high-frequency stimulation was nonlinear. Interestingly, the facilitation was sublinear at normal calcium concentrations (2.5 mM extracellular [Ca^{2+}]), but supralinear in physiological calcium concentrations (1.2 mM extracellular [Ca^{2+}]) [22] (Fig. 2B). The supralinearity of STF observed in 1.2 mM [Ca^{2+}] was caused by a switch from predominantly univesicular to predominantly multivesicular release. In contrast, multivesicular release was already in place in 2.5 mM [Ca^{2+}], and the facilitation observed under these conditions can be solely attributed to the recruitment of additional neurotransmitter release sites at the same synaptic bouton [22]. These two mechanisms, by which MF-PN synapses can facilitate glutamate release, arise from complex intra-bouton calcium dynamics [30, 51, 52], which lead to gradual and compartmentalized increases in calcium concentration. Consistent with the expectation that these two modes could lie on the opposite sides of the inverse-parabolic relationship between coefficient of variation (CV) and mean, normal calcium was associated with a gradual decrease of CV through stimulation, while physiological calcium was associated with an increase of CV (Fig. 2C). Perhaps because the TM model was based on experiments at 2 mM calcium concentration, the model emulates sublinear facilitation. Supralinear facilitation is not possible in the original structure of the model (Fig. 3C), as can be verified by mathematical inspection of the update equations (see Methods). Hence the TM model must be modified to capture the supralinear facilitation typical of experimental data at physiological calcium concentrations.

To extend the TM model to account for supralinear facilitation, we considered a small modification to the dynamics of facilitation without adding a new dynamic variable (Fig. 3A), although supralinear facilitation can be achieved with an additional state variable. This modification allows the facilitation variable of the TM model u to increase supralinearly when u is small, and sublinearly when u is large (see Methods). By lowering the baseline facilitation parameter U, the extended TM model switches from sublinear facilitation to a supralinear facilitation (Fig. 3D). We thus have shown that a modification to the set of equations for the TM model is required to present supralinear facilitation and capture the experimentally observed facilitation at physiological calcium.

In contrast, for the linear-nonlinear model framework, the switch from sublinear to supralinear facilitation does not require a modification to the equations. We can change sublinear facilitation into supralinear facilitation by lowering the baseline parameter without changing the efficacy kernel. When the baseline parameter is high, a facilitating efficacy kernel is likely to hit the saturating, sublinear, part of the nonlinear readout (Fig. 3E). When the baseline parameter is low, the same facilitating efficacy kernel can recruit the onset of the nonlinearity, which gives rise to supralinear facilitation (Fig. 3F). Thus, changes in extracellular calcium are conveniently mirrored by modification of a baseline parameter in the SRP model. Later in this manuscript, we expand the modelling framework to account for probabilistic synaptic transmission and demonstrate that the modification of the baseline parameter similarly explains the experimentally observed changes in CV.

Facilitation Latency

Next we illustrate the role of the efficacy kernel to generalize to the multiple timescales of STP without requiring a change in the structure of the model. As an illustrative example, focus on the one particular synapse showing facilitation latency [6]. In mossy fiber synapses onto inhibitory interneurons, the facilitation caused by a burst of action potentials increases during the first 2 seconds after burst (Fig. 4A). This delayed facilitation cannot be captured by the classical TM model because facilitation is modeled as a strictly decaying process and the experimental data show that facilitation

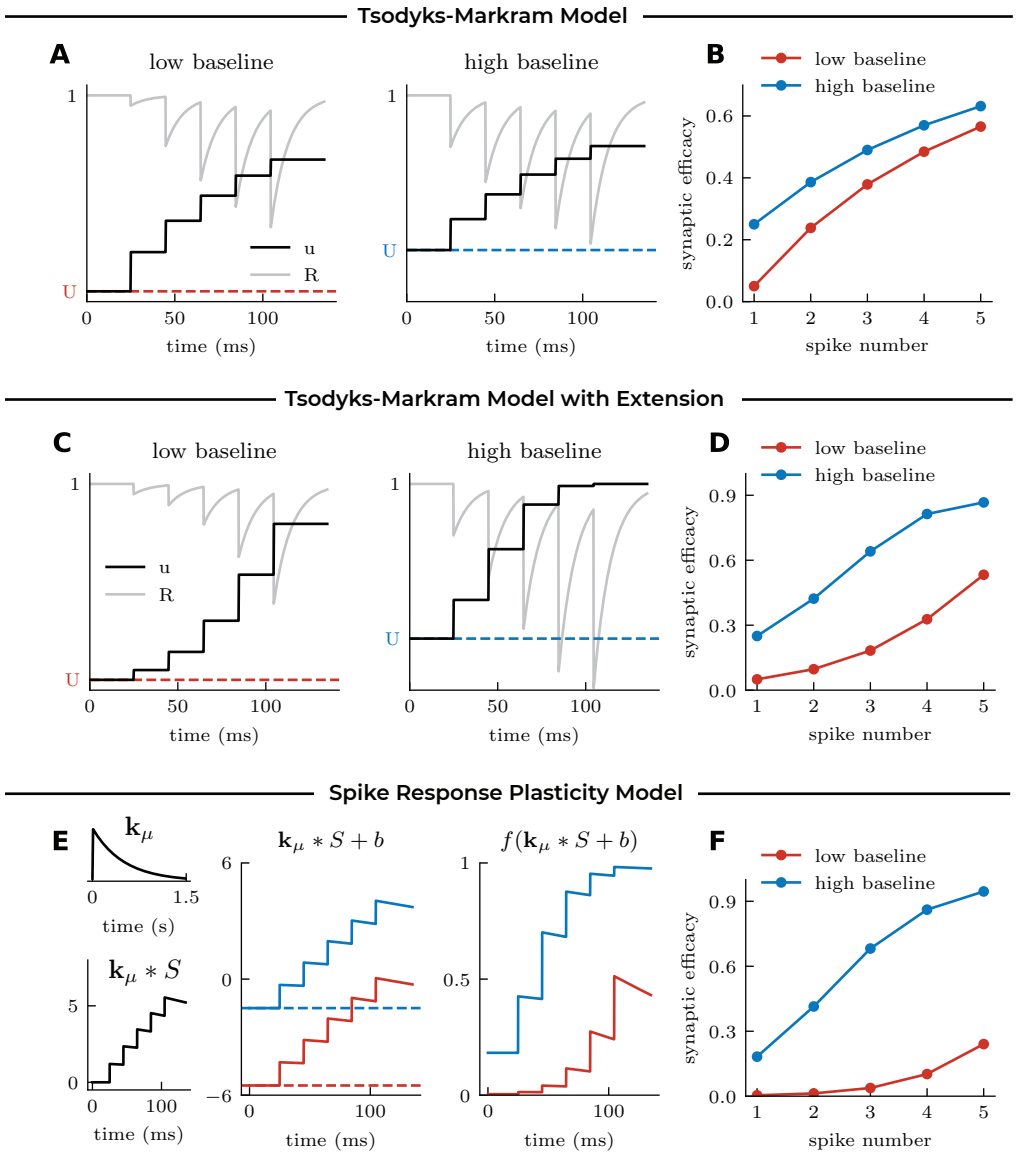

Fig 3. Modeling sublinear and supralinear facilitation through changes in the baseline parameter: **A** Mechanism of the classic TM model [24–26], illustrated in response to 5 spikes at 50 Hz for different values of the baseline parameter U. **B** Synaptic efficacy $u * R$ at each spike according to the classic TM model. Facilitation is always restricted to sublinear dynamics. **C** Mechanism and **D** Synaptic efficacy $u * R$ at each spike according to the extended TM model (see Methods). Choosing the baseline parameter U sufficiently small allows for supralinear facilitation. **E** Mechanism of the SRP model, illustrated for two different values of the baseline parameter b, with the same synaptic efficacy kernel k_μ (left). Changing the baseline parameter b leads to a linear displacement of the filtered spike train $k_\mu * S + b$ (middle), which causes a shift from sub- to supralinear dynamics after the nonlinear readout $f(k_\mu * S + b)$. **F** Resulting synaptic efficacy at each spike according to the SRP model. Changing the baseline parameter causes a switch from sublinear to supralinear facilitation, as observed experimentally in response to varying extracellular $[Ca^{2+}]$ (see Fig 2.)

increases during the first 1-2 seconds following a burst. Adding to this model a differential equation for the slow increase of facilitation is likely sufficient to capture facilitation latency, but this modification is considerable. In the linear-nonlinear framework, one could capture the facilitation latency by modifying the shape of the efficacy kernel. An efficacy kernel with a slow upswing (Fig. 4B), once convolved with a burst of action potentials followed by a test-pulse (Fig. 4C) will produce a delayed increase in synaptic efficacy (Fig. 4D) and match the nonlinear increase in facilitation with the number of stimulation spikes. Without automated fitting of the kernel to the data, a simple change to the efficacy kernel captures facilitation latency. The same model also captured the potentiation of amplitudes as a function of the number of action potentials in the burst (Fig. 4E). Thus, provided that the efficacy kernel is parameterized with basis function spanning a large part of the function space, the SRP model can aptly generalize to STP properties unfolding on multiple timescales.

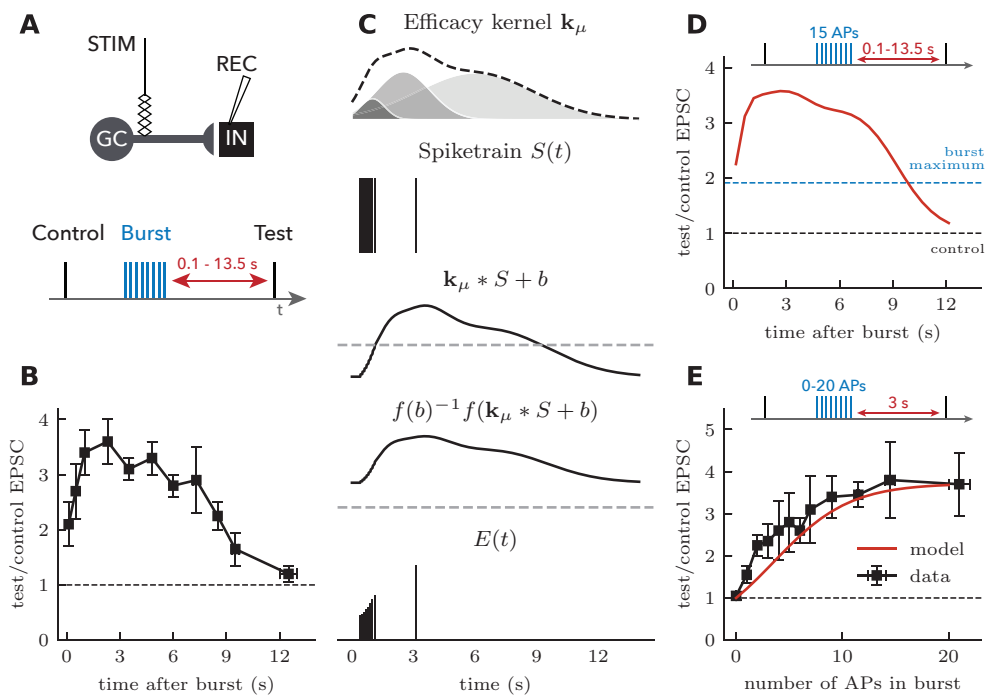

Fig 4. Post-burst facilitation captured by a delayed facilitation kernel: **A** Experimental setup and **B** measurement of post-burst facilitation in CA3 interneurons (redrawn from Ref. [6]). **C** Synaptic plasticity model. A delayed facilitation kernel was chosen as the sum of three normalized Gaussians with amplitudes {125, 620, 1300}, means {1.0, 2.5, 6.0} s and standard deviation {0.6, 1.3, 2.8} s. The spike train (8 spikes at 100 Hz followed by a test spike) is convolved with the delayed facilitation kernel. A nonlinear (sigmoidal) readout of the filtered spike train leads to synaptic efficacies. Dashed lines indicate zero. **D** Efficacies of test spikes in the synaptic plasticity model as a function of the number of action potentials in the preceding burst. **E** Synaptic efficacy of test spikes (3 s after a single burst at 160 Hz) as a function of the number of action potentials (APs). Data redrawn from Ref. [6].

Stochastic Properties

Synaptic transmission is inherently probabilistic. The variability associated with synaptic release depends intricately on stimulation history, creating a complex

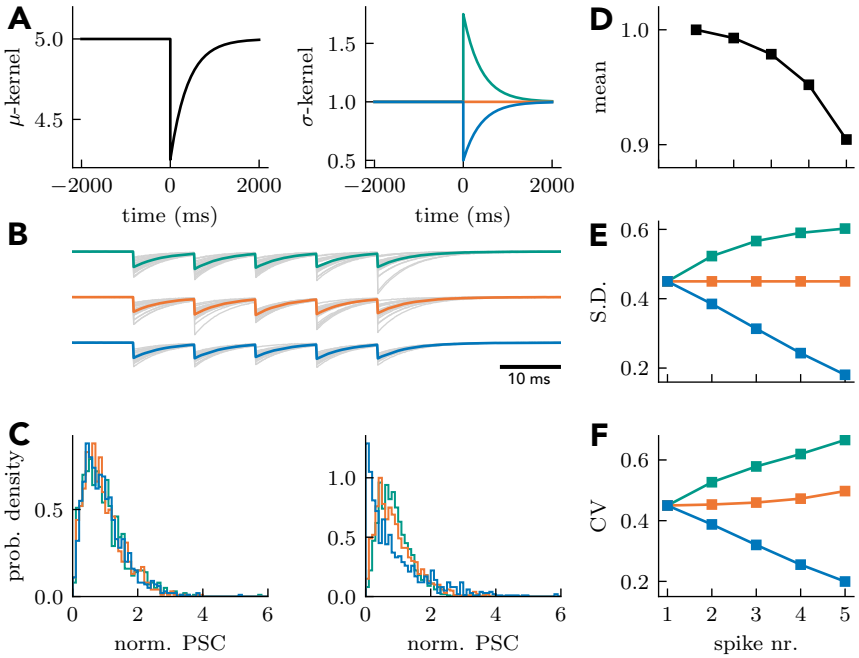

Fig 5. Capturing heteroskedasticity with a two-kernel approach. **A** The μ-kernel regulating the dynamics of the mean amplitude is paired with a σ-kernel regulating the dynamics of the variance. Three σ-kernels are shown: a variance increasing (teal), a variance invariant (orange) and a variance decreasing (blue) kernel. **B** Sample PSC responses to a spike train generated from the three σ-kernels (gray lines) along with the associated mean (full lines). **C** Probability density function of the amplitude of the first (left) and last (right) pulse. **D** The mean amplitude is unaffected by different σ-kernels. **E** The standard deviation is either increasing (teal), invariant (orange) or decreasing (blue), consistent with the polarity of the σ-kernel. **F** The coefficient of variation results from a combination of μ and σ kernel properties.

heteroskedasticity. Such changes in variability may be a direct reflection of history-dependent changes in amplitudes. Although a fixed relationship between the mean amplitude and the variance of synaptic responses could be expected if the only source of variability was a fixed number of equal-sized vesicles being randomly released with a given probability (a binomial model) [53], the variability should also depend on the dynamics of both the changing number of readily releasable vesicles and the changing probability with which they release [54]. In addition, other sources of variability are present such as the mode of release [55] or the size of vesicles [56, 57]. Figure 2C illustrates one type of heteroskedasticity observed experimentally whereby the variability increases through a stimulation train but only for the physiological calcium condition. To capture these transmission properties, we established a stochastic framework. Since the mechanisms underlying the dynamics of the variability of synaptic release are not known, we first constructed a flexible but complex model, and considered simplifications as special cases.

In the previous section, we treated the deterministic case, which corresponds to the average synaptic efficacies. We next considered a sample of synaptic efficacies to be a random variable such that the jth spike was associated with the random variable Y_j. Its

mean is given by the linear-nonlinear operation:

$$\langle Y_j \rangle \equiv \mu_j = \frac{1}{f(b)} f\left(\mathbf{k}_\mu * S(t_j) + b\right). \tag{4}$$

In this way, the current trace is made of PSCs of randomly chosen amplitudes whose average pattern is set by the efficacy kernel: $I(t) = \sum_j y_j \mathbf{k}_{PSC}(t - t_j)$, where y_j is an instance of Y_j. Sampling from the model repeatedly will produce slightly different current traces, as is typical of repeated experimental recordings (Fig. 2A).

To establish stochastic properties, we had to select a probability distribution for the synaptic efficacies. Previous work has argued that the quantal release of synaptic vesicles produces a binomial mixture of Gaussian distributions [53, 58]. There is substantial evidence, however, that releases at *single synapses* are better captured by a mixture of skewed distributions such as the binomial mixture of gamma distributions [56, 59]. Such skewed distributions are also a natural consequence of Gaussian-distributed vesicle diameters and the cubic transform of vesicle volumes [57]. For multiple synaptic contacts, release amplitudes should then be captured by a weighted sum of such binomial mixtures, a mixture of mixtures as it were. Indeed, a binomial mixture of skewed distributions has been able to capture the stochastic properties of PSC amplitudes from multiple synaptic contacts [27, 60], but only under the assumption that each synapse contributes equally to the compound PSC. Together, these considerations meant that for a simple parameterization of the random process, we required a skewed distribution whose mean and standard deviation could change during the course of STP.

Following prior work [56, 60], we chose to focus on gamma-distributed PSCs:

$$p(y_j | S(t_j), \theta) = g(y_j | \mu_j, \sigma_j), \tag{5}$$

where $g(y|\mu, \sigma)$ is the gamma distribution with mean, μ, and standard deviation, σ. Here we assume statistical independence of successive response, $p(y_j, y_{j-1}|S, \theta) = p(y_j|S, \theta)p(y_{j-1}|S, \theta)$. The mean is set by the linear-nonlinear operation (Eq. 4) and the standard deviation is set by a possibly distinct linear-nonlinear operation:

$$\sigma_i = \sigma_0 f(k_\sigma * S_i + b_\sigma), \tag{6}$$

where we introduced a baseline parameter, b_σ and another kernel, k_σ, for controlling the standard deviation. We call this time-dependent function, the variance kernel. The factor σ_0 is introduced to scale the nonlinearity f appropriately, but could be omitted if data has been standardized. In this framework, some common statistics have a simple expression in terms of model parameters. This is the case for the stationary CV. Since we are considering filters decaying to zero after a long interval and amplitudes normalized to the responses after long intervals, we have CV $= \sigma_1/\mu_1 = \sigma_0 f(b_\sigma)$.

This stochastic model has two important special cases. The first is the case of constant variance, which is obtained by setting the variance kernel to zero. In that case the CV of releases will be inversely proportional to the mean given in Eq. 4, and thus in agreement with experimental data in 2.5 mM Calcium (Fig. 2C). The other case corresponds to variability that is proportional to the mean. In the second case, we assumed that the dynamics of variability followed the dynamics of the mean amplitude. For this, we set $\mathbf{k}_\sigma = \mathbf{k}_\mu$. Although both mean and variance were modeled with the same kernel, different baseline parmeters can give rise to different dynamics of the CV. Both these simplifications are of interest because they drastically reduce the number of parameters in the model.

The properties of this choice of probability distribution are illustrated in Figure 5. Using a depressing kernel, Fig. 5 depicts the effect of choosing a variance kernel with

positive, negative and zero amplitude (Fig. 5A). These kernel choices show that the model can capture both increases and decreases of variability, although an increase in variability during STD is generally observed [54, 61]. The temporal profile of the variance kernel determines the time-dependent changes in variance. For simplicity, we chose an exponential decay with a relaxation time scale equal to that of the efficacy kernel. The kernel amplitude and baseline were chosen to match experimental observations at STD synapses (CV increasing from a little less than 0.5 to almost 1 after 5 pulses [54]). With these modeling choices, we simulated the probabilistic response to input trains (Fig. 5B, 5 spikes, 100 Hz). The model with positive σ-kernel shows a progressive increase of trial-to-trial variability. Conversely, the model with a negative σ-kernel displays the opposite progression, as can be observed by comparing the probability distribution of the first and the last response (Fig. 5C). The average response follows precisely the same STD progression (Fig. 5D), despite drastically different progression of standard deviation (Fig. 5E) and CV (Fig. 5F). Thus gamma-distributed amplitudes with dynamic variance can capture multiple types of heteroskedasticity.

Next we asked if the model could capture the striking changes in heteroskedasticity observed in MF-PN synapses (Fig. 2C). In this case, decreasing the extracellular concentration of calcium not only changed the average response progression from sublinear to supralinear (Fig. 2B), but also changed the CV progression from strongly decreasing to strongly increasing (Fig. 2C, [22]). Figure 6 shows that changing the μ-kernel baseline in a model with facilitating standard deviation can reproduce this phenomenon. Here, as in the deterministic version of the model, the change in baseline changes the progression of efficacies from sublinear to supralinear (Fig. 6A-D). These effects are associated with changes in variances that are sublinear and supralinear, respectively (Fig. 6E). In the model with a low baseline (red curve in Fig. 6), the variance increases more quickly than the efficacy, leading to a gradual increase in CV. Despite the fact that the variance increases for both cases (Fig. 6E), only the model with sublinear increase in efficacy displays a decreasing CV. We conclude that, by controlling a baseline parameter, the model can capture both the change from sublinear to supralinear facilitation and the change in heteroskedasticity incurred by a modification of extracellular calcium.

Inference

Thus far, we have illustrated the flexibility of the SRP framework for qualitatively reproducing a diversity of notable synaptic dynamics features. Now we investigate the ability of this framework to capture synaptic dynamics quantitatively. As in the characterization of cellular dynamics [62], a major impediment to precise characterization is parameter estimation. As efficient parameter inference largely depends on the presence of local minima, we first investigated the cost function landscape for estimating model parameters.

We have developed an automatic characterization methodology based on the principle of maximum likelihood (see Methods). Given our probabilistic model of synaptic release, we find optimal filter time-course by iteratively varying their shape to determine the one maximizing the likelihood of synaptic efficacy observations. The method offers a few advantages. First, the method is firmly grounded in Bayesian statistics, allowing for the inclusion of prior knowledge and the calculation of posterior distributions over the model parameters [26, 60]. Second, although targeted experiments can improve inference efficiency, our approach does not rely on experimental protocols designed for characterization. Naturalistic spike trains recorded in-vivo [30, 63], Poisson processes or other synthetic spike trains can be used in experiments to characterize synaptic dynamics in realistic conditions.

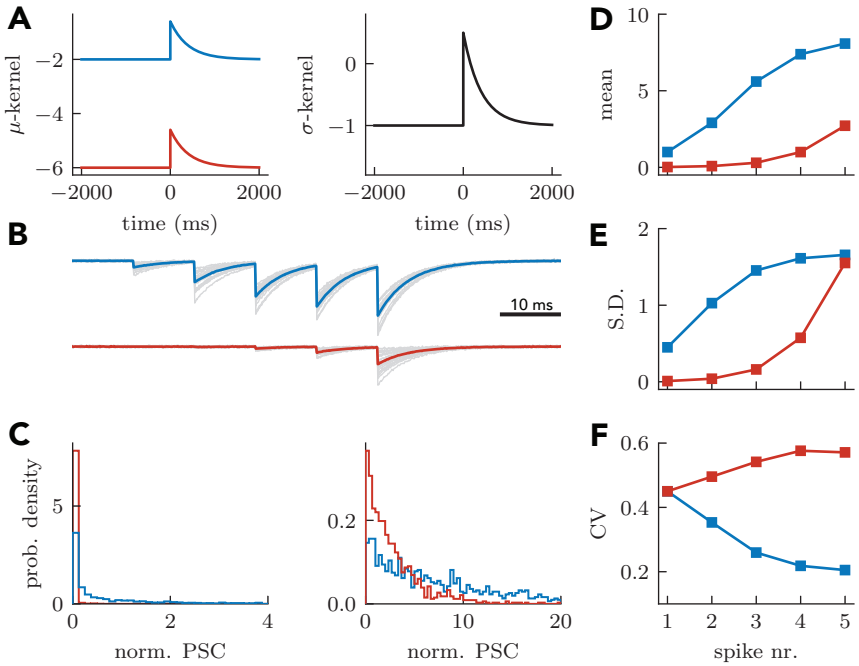

Fig 6. Capturing effect of external calcium concentration on coefficient of variation through baseline of μ-kernel. **A** Comparing facilitating μ-kernels with high (blue) and low (red) baseline but fixed, σ-kernel. **B-F** as in Fig. 5. The coefficient of variation increases with pulse number for the low baseline case, but decreases with pulse number for the high baseline case.

We treat the number of basis function as well as the timescale (or shape) of the basis functions for efficacy and variance kernel as meta-parameters. Such meta-parameters are considered part of the fitting procedure, rather than a characteristic of the mechanistic model. We emphasize this point because, although we have parametrized the efficacy kernel as a sum of exponential decays, each characterized by a specific timescale (see Methods), we do not expect that any of these timescales match the timescale of a specific biological mechanism. One reason for this comes from the fact that it is possible to capture reasonably well a mono-exponential decay with a well chosen bi-exponential decay. Thus, a single biological timescale can be fitted by the appropriate combination of two timescales. Together, some heuristics can be applied as to the number and the choice of timescale that we expect to see in a particular system (e.g. timescales faster than 1 ms are stimulus artefacts and longer than 1 min would be long-term plasticity), but the choice of meta-parameters should be guided by the properties of statistical inference: choosing either a small number of well-spaced timescales to avoid overfitting, or a very large number of timescales so as to exploit the regularizing effect of numerous parameters [35, 64, 65].

To test the efficiency of our inference method, we generated an artificial Poisson spike train with 4000 spikes at an average firing rate of 10 Hz and used this spike train to generate surrogate synaptic efficacy data using our SRP model (Fig. 7A-B). We then asked if our inference method identified the correct parameters and whether local minima were observed. Instead of the case where the filters are described by a combination of nonlinear basis functions, we considered only one basis function, a mono-exponential decay, with its decay time constant known. In cases where the time constant is unknown, one would fit the coefficient of a combination of nonlinear basis

functions, as is typical in other linear-nonlinear models [32, 34, 66, 67]. Using a long stimulus train, the likelihood function appeared convex over a fairly large range of parameter values, as no local minima were observed (Fig. 7C-F). The slanted elongation of likelihood contour indicates a correlation or anti-correlation between parameter estimates. Not surprisingly, we found that the estimates of baseline and scale factor of the σ-kernel would be anti-correlated (Fig. 7D), while on the other hand the estimates of filter amplitudes for efficacy and variance would have a correlation (Fig. 7C). To test how many training spikes would be needed for accurate parameter inference, we simulated Poisson spike trains of different lengths and used gradient descent on the likelihood function to infer all model parameters (see methods). We found that the parameter estimates matched closely the parameters used to simulate the responses after 100-200 spikes (Fig. 7G-H), with more training spikes leading to better parameter estimation. The relationship between error in parameter estimation and training size is such that for large training sets the percent error goes to zero (Fig. 7G and H). Using a separate artificial Poisson input for testing the predictive power of the model, we calculated the mean squared error between the inferred and true model (Fig. 7I). The prediction error of the inferred model almost matched that of the true model, even if inference was based on less than 100 spikes. We conclude that maximum likelihood applied to surrogate data is able to characterize the model efficiently and accurately, and that, for simple filters, the landscape is sufficiently devoid of local minima to allow efficient characterization.

Model Validation on Mossy Fiber Synapses

Having established a method to infer model parameters, we now fit the model to experimental data and evaluate its accuracy for predicting the PSP amplitude to stimulation protocols that were not used for training. Furthermore, to serve as a benchmark, we will compare predictions from the SRP model with those of the TM model. To do this, we used data from the mossy fiber synapse where a total of 7 different stimulation protocols were delivered and the resulting PSP amplitude were recorded: 10x100 Hz (Fig. 8A), 10x20 Hz, 5x100 Hz + 1x20 Hz, 5x20 Hz + 1x100 Hz, 5x100 Hz + 1x10 Hz, 111 Hz and an in vivo recorded spike train from dentate gyrus granule cells. This experimental data was acquired at 1.2 mM extracellular [Ca^{2+}] in P17 - 25 male rats (See Ref. [30] for the complete experimental protocol).

Before assessing prediction accuracy, we scrutinized the model parameters fitted to all of the protocols. The optimal SRP model for this synapse had a slightly negative baseline ($b_\mu = -1.91$) and a net positive efficacy kernel which extended on multiple timescales (Fig. 8B, $\theta_\mu = [7.6, 11.8, 277.0]$ for three exponential decays with time constants $\tau = [15, 100, 650]$ ms). This captures well the fact that these synapses are known to be facilitating and that multiple timescales of facilitation have been reported [22]. These parameters reproduced perfectly the nonlinear progression of EPSC amplitude in response to 20 Hz and 100 Hz train (Fig. 8C).

We have also validated one of the assumptions of the stochastic model, the independence of variability through subsequent sampling (Eq. 5). To test this, we calculated the noise correlation across subsequent stimulation times. Figure 8D shows the deviation around the trial-averaged amplitude for one stimulation time against the deviation around the trial-averaged amplitude for the next stimulation time. Across all such amplitude pairs in the data ($n = 12040$), we found a small, but significant correlation ($r = 0.04$, $p < 0.001$). Based on the small correlation coefficient, we concluded that the effect of previous stimulation on the variability of response amplitudes is negligible and thus the model assumptions hold.

We then considered the σ-kernel found by the fitting method to capture changes in response variability. The optimal kernel was very similar (Fig. 8E) to the optimal

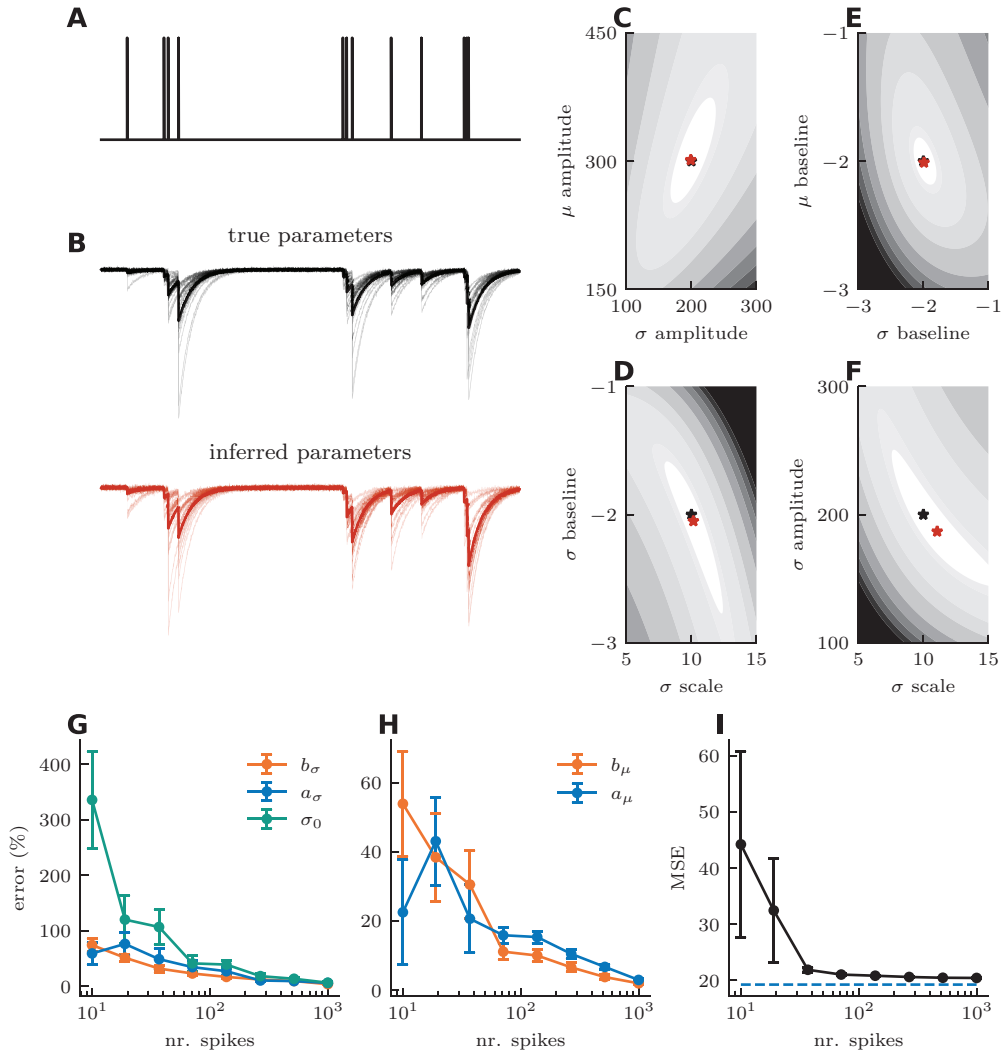

Fig 7. Statistical inference of kinetic properties on surrogate data. **A** Simulated Poisson spike trains mark pre-synaptic stimulation. **B** Simulated post-synaptic currents of the spike train in A for independent sampling (thin black lines) and mean efficacy (thick black line) of the true parameter set (top) and of the inferred parameter set (bottom). **C**-**F** Negative log-likelihood landscape, true parameters (black stars) and function minima (red stars) as a function of **C** μ- and σ-kernel amplitudes, **D** σ baseline and scaling factor, **E** μ and σ baseline and **F** σ scaling and amplitude. **G** Average σ parameter errors as function training size. **H** average μ parameter errors as a function of training size (right). **I** Mean square error (MSE) of the inferred and model on an independent test set as a function of training size. Dashed line is MSE between independent samples of the true parameter set.

μ-kernel. Both were starting from a slightly negative baseline and were made of multiple timescales, composed mostly of the fastest and slowest timescale ($b_\sigma = -1.59$, $\theta_\sigma = [11.9, 10.1, 271.6]$ for exponential decays with time constants $\tau = [15, 100, 650]$ ms). These allowed the SRP model to adequately capture the nonlinear progression in EPSC variability through the stimulation of 20 Hz and 100 Hz trains (Fig. 8F).

Next, we separated the data into training and test sets and only optimized the model

parameters on the training set. To separate the data, we held out the data from one stimulation protocol and predicted its responses using parameters optimized on all of the other protocols. We repeated this procedure 7 times, holding out each stimulation protocol, and performed the same model optimization for both SRP and TM models. Figure 8G shows a subset of model predictions compared with observed mean amplitude. Consistent with the fact that the TM model cannot capture the supralinear increase observed after the first few stimulations at high frequency (Fig. 3), the SRP model systematically outperformed the TM model for the prediction the first few stimulations. In addition, the in-vivo-like stimulation pattern was well captured by the SRP model, except for the last stimulation time that both SRP and TM models failed to predict.

To test whether the SRP model would consistently outperform the TM model, we implemented a bootstrapping procedure with 20 randomly re-sampled subsets of the data. To obtain each subset, we randomly excluded 20% of traces from every stimulation protocol. For each subset of data, we then iteratively held out each stimulation protocol, as described in the previous paragraph. This procedure results in a total of 7 TM and SRP model fits (each stimulation protocol withheld) for each of the 20 bootstrap iterations. To quantify the prediction accuracy across all held out protocols, we calculate the mean squared error (MSE). Like all metrics, the MSE weighs some features of the response more than others. Here, since later stimulations in a train are generating larger amplitudes and, therefore, larger errors, the later stimulations are weighted more than the first stimulations. Since the TM model is systematically worse on the stimulations early in the train (in part because the TM model uses MSE for parameter inference), this metric should favour the TM model. We found that, using a metric favourable to the TM model, the SRP model was more accurate in capturing both training data (paired sample t-test, $T = 45.5$ $p < 0.001$) and held out testing data (paired sample t-test, $T = 10.5$ $p < 0.001$), achieving a root mean squared error of 9.6 (Fig. 8H) across all stimulation protocols, only slightly above the MSE due to intrinsic variability (dashed line in Fig.8H). The small increase in test error from the training error indicated that some overfitting may be present in both models. Since the SRP model has more parameters (8 parameters in the SRP model with 3 basis functions versus 4 parameters in the TM model), overfitting can account for its better training error but not for the better test error. Together, we found that the SRP model predicts the response to novel stimulation patterns with high accuracy, and outperforms the TM model.

Relation to Generalized Linear Models

We have shown that, in one situation, the likelihood landscape appears devoid of local minima, but is this always the case? Without additional restrictions on the model described in the previous section, it is unlikely that the likelihood would be always convex. However, with some simplifications, the model becomes a Generalized Linear Model (GLM), which is a class of model that has been studied in great detail [41, 68–70]. In this section, we describe two such simplifications.

We can assume that the standard deviation is always proportional to the mean: $\boldsymbol{\sigma} = \sigma_0 \boldsymbol{\mu}$. This assumes that the CV is constant through a high-frequency train, a coarse assumption given the large changes in CV observed experimentally [22, 54]. If for some reason an accurate reproduction of the changes in variability can be sacrificed, this simplification leads to interesting properties. In this case, no variance parameters are to be estimated apart from the scaling σ_0. There is thus a reduction in the number of parameters to be estimated. In addition, since the gamma distribution belongs to the exponential family and the mean is a linear-nonlinear function of the other parameters, we satisfy the requirements for GLMs. In some similar models, the likelihood function is convex [41], but since this is not the case in general [69], parameter inference must

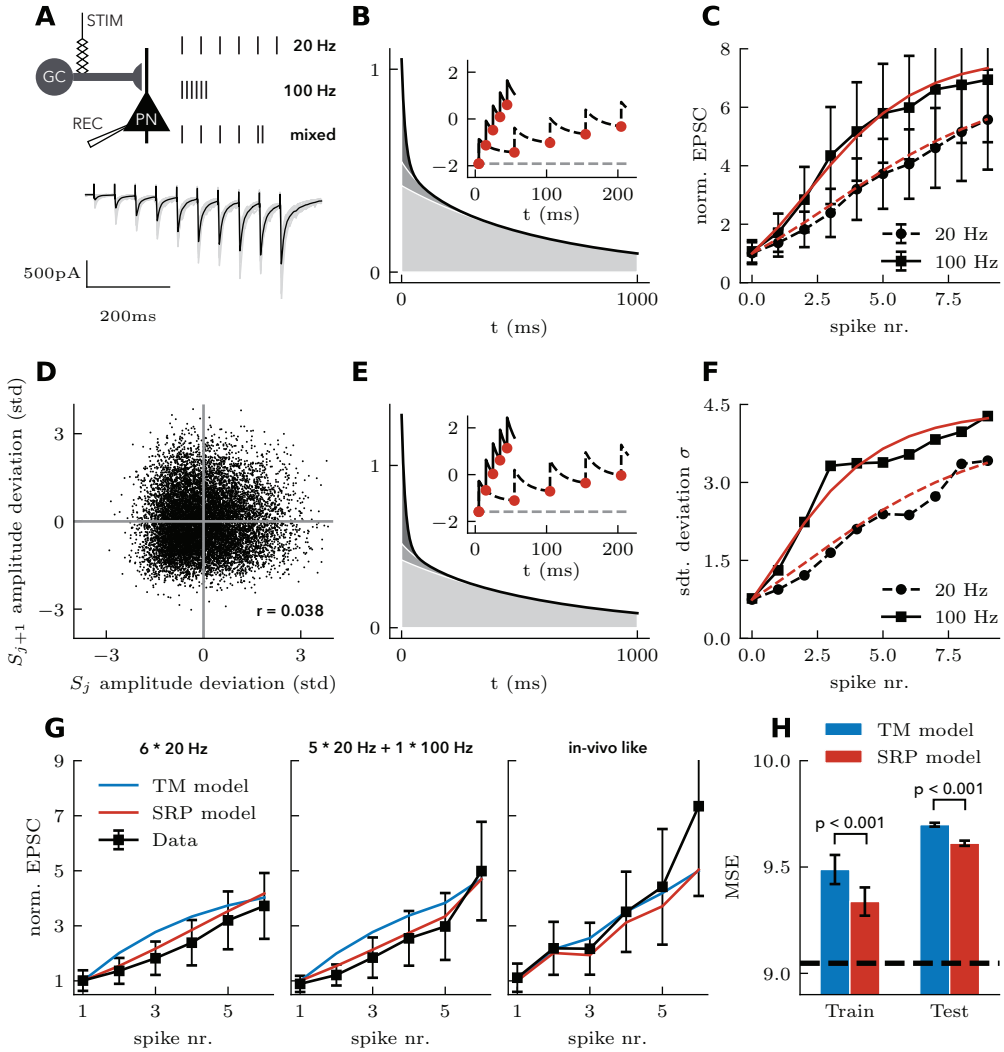

Fig 8. Experimental validation of the SRP model. **A** Experimental schematic (top) and representative EPSCs recorded from CA3 pyramidal cells in response to stimulation of mossy fibers (bottom). **B** Optimal efficacy kernel (black line) is made of the combination of three exponentially decaying functions (shades of gray) with time constants $\tau = [15, 100, 650]$ ms. Inset shows the quantity $\mathbf{k}_\mu * S + b_\mu$ in response to 100 Hz (full black line) and 20 Hz (dashed black line) train. Circles indicate times where the nonlinear readout is taken and the dashed gray line indicates the baseline. **C** Normed PSC for SRP model (red lines) and data (black lines) for the regular 20 Hz (dashed lines) and 100 Hz (full lines) protocols. **D** Experimental EPSC amplitude deviation (difference between an observation and its trial average) against the previous EPSC amplitude deviation. **E** Optimal σ-kernel and illustration of $\mathbf{k}_\sigma * S + b_\sigma$. **F** As in **C** but showing the standard deviation. **G** Predictions of stimulation protocols held out from training. TM model (blue) and SRP model (red) predictions are shown with data (black) for the 20 Hz stimulation (left), 5x20 Hz+1x100 Hz stimulation (center) and in-vivo like stimulation (right). **H** Mean squared error (MSE) of models (bars) and variance of the data (dashed line), averaged across stimulation protocols.

control for the robustness of solutions.

For the depressing synapses, the CV is increasing during a high-frequency train. This can be modeled by a constant standard deviation with a mean decreasing through the stimulus train. Similarly, for the facilitating synapses at normal extracellular calcium shown in Fig. 2, the gradual decrease in CV can be explained by an approximately constant standard deviation, $\boldsymbol{\sigma} = \sigma_0$, and an increasing mean. Setting the variance to a constant again reduces the number of parameters to be estimated and recovers the necessary assumptions of a GLM.

Relation to Convolutional Neural Networks with Dropout

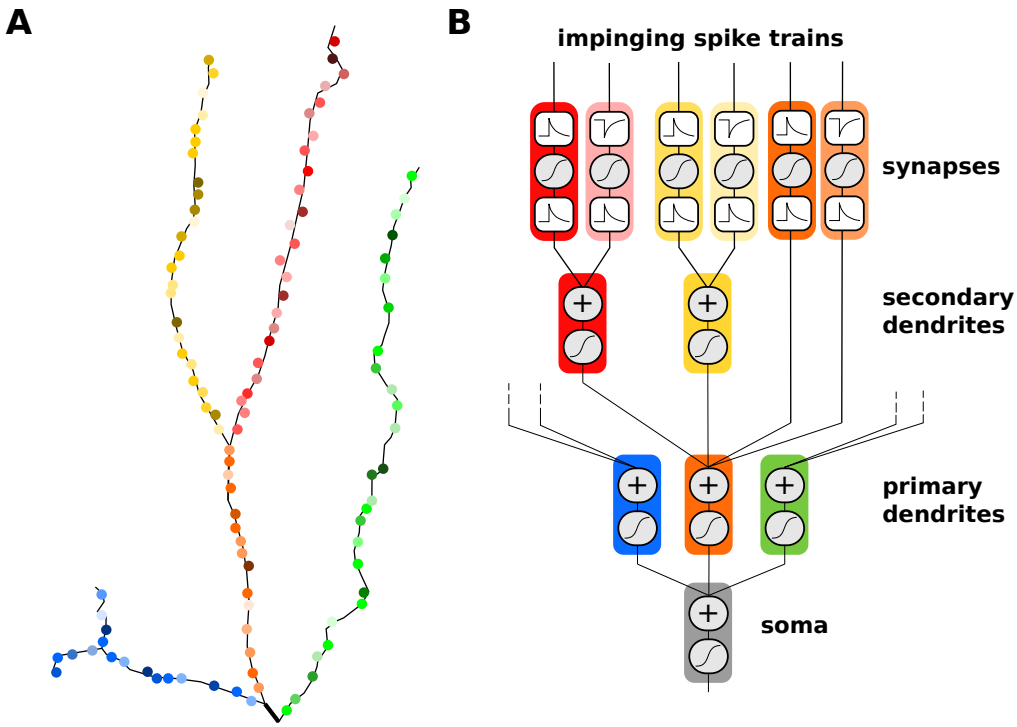

Fig 9. A synaptic contribution to the hierarchy of linear-nonlinear computations. **A** Synapses distributed on primary (orange, blue and green) and secondary (yellow and red) dendrites may have different synaptic properties (different color tints). **B** Each synapse is characterized by two kernels separated by a nonlinear sampling operation. 1) A pre-synaptic convolution kernel regulates synaptic dynamics. 2) A post-synaptic convolution kernel regulates the shape of the post-synaptic potential locally. The post-synaptic potentials from different synapses are summed within each dendritic compartment, forming a processing hierarchy converging to the soma.

A convolution followed by a nonlinear readout is also the central operation performed in convolutional neural networks (CNNs). Because this type of algorithm has been studied theoretically for its information processing capabilities and is associated with high performance in challenging tasks, we describe here one mapping of the biological models of information processing onto a model of the type used in artificial neural networks. Our main goal is to relate our SRP model with models in the machine learning literature.

CNNs are often used on images, and such inputs are conceived in two spatial dimensions but CNNs on data with a single temporal dimensions offer a more straightforward relationship with the properties of short-term plasticity. Such CNNs consider an input arranged as a one-dimensional array $\mathbf{x}$, which is convolved with a bank of kernels $\{\mathbf{k}_i\}$ and readout through a nonlinearity f to generate the activity of the first layer of 'hidden' neural units

$$h_t^{(i)} = f\left(\mathbf{k}_i^T(\mathbf{m} \odot \mathbf{x}_{t:t+K})\right) \tag{7}$$

where K_i is the length of the ith kernel in the bank. The convolution is here implied by the matrix multiplication, which applies to a section of the input and is shifted with index t. The bank of kernels extracts a number of different features at that neural network layer.

In Eq. 7, we have added a mask $\mathbf{m}$ which operates on the input with the Hadamard product ($\odot$). This mask is introduced to silence parts of the input, randomly and ensure that learning yields kernels robust to this type of noise, an approach called *dropout* [71]. It is made of samples from Bernoulli random variable normalized so that the average of $\mathbf{k}_i^T(\mathbf{m} \odot \mathbf{x}_{t:t+K})$ is $\mathbf{k}_i^T \odot \mathbf{x}_{t:t+K}$.

Although CNN architectures vary, the next layer may be that of a pooling operation

$$h_k^{(i)} = \frac{1}{Z}\sum_{t=k}^{k+Z} h_t^{(i)}$$

where Z is the pooling size, in number of time steps. Then these activities reach a readout layer for predicting higher-order features of the input

$$y_k = f\left(\mathbf{w}^T\mathbf{h}_k\right) \tag{8}$$

where the vector $\mathbf{w}$ weighs the pooled activities associated with the different kernels in the filter bank. By optimizing the kernels $\mathbf{k}$ and weights $\mathbf{w}$, similar CNNs have been trained to classify images [71,72] as well as sounds [73,74].

In a synapse with STP, the discretized efficacy train of the ith afferent, $\mathbf{e}_t^{(i)}$, results from a convolution and a nonlinear readout of the discretized spike train $\mathbf{s}_t^{(i)}$

$$e_t^{(i)} = f\left(\mathbf{k}_i^T\mathbf{s}_{t:t+K}^{(i)}\right)\mathbf{s_t}^{(i)}, \tag{9}$$

which maps to a discretized version of the continuous time SRP model in Eq. 2 and 3. By comparing with Eq. 7, this equation (Eq. 9) makes clear the parallel with a convolutional layer. Here, the spike train is conceived as a stochastic random variable sampling a potential [34,48,49]. Thus, the stochastic spike train is analogous to the dropout mask, $\mathbf{m}$. The efficacy train triggers PSCs, which are pooling the efficacy train on the PSC : $e_k^{(i)} = \sum_{t=k}^{k+Z} \epsilon_{t-k} e_t^{(i)}$, where ϵ_i is a discretized and normalized PSC. Then, different synaptic afferents, with possibly different efficacy kernels (Fig. 9), are combined with their relative synaptic weights before taking a nonlinear readout at the cell body [34,49] or the dendrites [75] to give rise to an instantaneous firing rate ρ_t:

$$\rho_t = f\left(\mathbf{w}^T\mathbf{e}_t\right) \tag{10}$$

This equation corresponds to the fully connected layer that followed a pooling operation, Eq. 8. Together, we find a striking parallel between the formalism developed here to describe STP and that of an artificial neural network by ascribing a number of biological quantities to concepts in artificial intelligence. A number of these parallels have been made in the literature: Stochastic firing as a dropout mechanism [71], PSP as a pooling operation in time, and synaptic weights as connection weights. In addition, we find that the SRP model introduces a bank of temporal kernels with their nonlinear readout, which makes explicit that single neurons act as multi-layer neural network even in the absence of dendritic processing.

Discussion

The linear-nonlinear framework has been able to capture core elements of subcellular [47], cellular [34, 36, 37, 76] and network signalling. We have shown that the same framework aptly captures synaptic dynamics. In the SRP framework, activity-dependent changes in efficacy are captured by an efficacy kernel. We have shown that switching the polarity of the kernel captures whether STD or STF is observed. Extending previous work at ribbon synapses [77], we have shown that the modelling framework captures multiple experimental features of synaptic dynamics. The SRP model presents three sources of added flexibility with respect to the well-established TM model: 1) an efficacy kernel with an arbitrary number of timescales, 2) a nonlinear readout with both supra- and sub-linear regimes, and 3) an additional kernel allowing for independent dynamics of variability. The model successfully predicted experimentally recorded synaptic responses to various stimulation protocols, and reproduced the changes in variability incurred by changing the levels of extracellular calcium. The framework can also naturally capture long-lasting effects such as post-burst facilitation. Finally, by considering the dynamics of stochastic properties, a maximum likelihood approach can estimate model parameters from complex, time-limited, and physiological stimulation patterns. The added flexibility and the efficient inference are of interest to large scale characterization of synaptic dynamics [78] as well as the understanding information processing in neural networks [15, 79].

When summarizing dynamic properties with two time-dependent functions we called kernels, we were compelled to ask what was their biophysical implementation? By analogy with characterization of neuronal excitability, the answer is likely to involve a mixture of independent mechanisms. The membrane kernel, for instance, depends on membrane resistance and membrane capacitance, but also the density of low-threshold channels, such as A- and H-type currents. Similarly, the efficacy kernel is likely to reflect residual presynaptic calcium concentration and the changing size of the readily releasable pool [31] but also many other possible mechanisms. Determining the relative importance of these processes, however, is not possible with the methodology described here. This could be achieved only with a combination of experiments aimed at isolating independent mechanisms and a detailed biophysical model, at the cost of constructing a model with reduced predictive power. Our modeling framework is not presented as a tool for identifying molecular mechanisms, but rather as one for characterization, network simulation, and theoretical analysis [25, 80, 81] of the diversity of synaptic dynamics across signalling pathways [17], cell types [14, 50] or subcellular compartments [82].

There remain limitations to this approach such as the choice of a gamma distribution of release sizes. Formally, this modeling choice means that we have replaced release failures with small to very small releases. In other terms, whereas the presence of release failures is a bimodal or multimodal distribution of amplitudes, the model assumes that the distribution of evoked amplitudes is unimodal. Nonetheless, recent work has shown that the release size distribution appears unimodal despite being generated by multiple modes [56]. We have argued that for the small vesicle sizes at central synapses, quantal peaks are smeared by quantal variability [56]. When considering electrophysiological preparations where multiple synapses are simultaneously activated [27, 60, 83], the diversity of synaptic weights will strengthen further the assumption for a gamma-distributed, right-skewed and unimodal distribution.

Another related question is that, having explored various monotonic progressions of variability, will the model capture a non-monotonic progression? This case is relevant because the random and equally likely release of a number of vesicles will give rise to a non-monotonic progression of variability when release probability is changing over a larger range. For instance, in a facilitating synapse where multiple release sites increase

an initially low release probability through a high-frequency train, the variability will first increase and then decrease. This convex, non-monotonic progression arises from the fact that variability is at its lowest point either when release probability is zero or when it is one. Given the mathematical features of the model, it may be possible to generate such a non-monotonic progression of variability with a biphasic σ-kernel.

Previous modeling and experimental work has established that dendritic integration can follow a hierarchy of linear-nonlinear processing steps [47, 75, 84]. Subcellular compartments filter and sum synaptic inputs through an integration kernel encapsulating local passive and quasi-active properties. Active properties are responsible for a static nonlinear readout and for communication toward the cell body. Much in the same spirit, the work presented here extends this model by one layer, where presynaptic spikes first pass through a linear-nonlinear step before entering dendrites (Fig. 9). Since synapses at different locations or from different pathways may have different synaptic dynamics [17, 82], and since spiking neural codes can multiplex streams of information [8, 85, 86], these synaptic properties have the capability to extract different streams of information from multiple pathways and to process these possibly independent signals in segregated compartments.

The structure of information processing arising from this picture bears a striking resemblance with multi-layer convolutional neural networks [87, 88]. But it should be noted that the convolution takes place along the temporal dimension instead of the spatial dimension for many neural network applications. Yet, this algorithmic similarity suggests that a linear-nonlinear structure of synaptic processing capabilities is shared between neural and neuronal networks. Whether the STP is controlled by genes [89], activity-dependent plasticity [90, 91], retrograde signalling [92], or neuromodulation [93, 94], a particular choice of efficacy kernels, when combined with a nonlinear readout, can optimize information processing as in Refs. [8, 95, 96].

Methods

All models, numerical simulations and parameter inference procedures were implemented in Python using the SciPy [**?**] and NumPy [**?**] packages and are publically available on GitHub (https://github.com/nauralcodinglab/flexible-stp).

Tsodyks-Markam Model and its Modifications

The Tsodyks-Markram (TM) model was first presented in 1997 [24] as a phenomenological model of depressing synapses between cortical pyramidal neurons and was quickly extended to account for short-term facilitating synapses [11, 50]. In the TM model, the normalized PSC amplitude μ_n at a synapse caused by spike n of a presynaptic spike train is defined as:

$$\mu_n = R_n u_n, \tag{11}$$

where two factors u_n and R_n describe the utilized and recovered efficacy of the synapse, respectively. The temporal evolution of these variables are described by the following ordinary differential equations:

$$\frac{dR(t)}{dt} = \frac{1 - R(t)}{\tau_R} - u(t^-)R(t^-)S(t) \tag{12}$$

$$\frac{du(t)}{dt} = \frac{U - u(t)}{\tau_u} + f\big[1 - u(t^-)\big]S(t), \tag{13}$$

where f is the facilitation constant, τ_u the facilitation time scale, U the baseline efficacy and τ_R the depression timescale. The spike-dependent changes in R and u are

implemented by the Dirac delta function within the spike train $S(t)$. The notation t^- indicates that the function should be evaluated as the limit approaching the spike times from below.

In the TM model, facilitation is modelled as spike-dependent increases in the utilized efficacy u. Immediately after each spike, the efficacy increases by $f(1-u(t^-))$. This efficacy jump depends on a facilitation constant f and on the efficacy immediately before the spike $u(t^-)$. Therefore, as u increases during a spike train, the spike-dependent 'jump' decreases for each subsequent spike. As a consequence, TM models of facilitating synapses are limited to a logarithmically saturating – that is, sublinear – facilitation.

To allow supralinear facilitation, we introduce a small change in the spike-dependent increase of factor u:

$$\frac{du(t)}{dt} = \frac{U-u(t)}{\tau_u} + u(t^-)f\left[1-u(t^-)\right]\delta\left(t-t_S\right). \tag{14}$$

In this new model, given a presynaptic spike train at constant frequency, the size of the spike-dependent jump $u(t^-)f\left[1-u(t^-)\right]$ saturates logarithmically for $u > 0.5$ but is increasing exponentially while $u < 0.5$. Thus this model provides supralinear facilitation in the low efficacy regimen, and it switches to sublinear facilitation for larger efficacies.

These models can be integrated between two spikes n and $n+1$, separated by time Δt to speed up the numerical implementation [50]. For the classic TM model we have

$$R_{n+1} = 1 - \left[1 - R_n\left(1-u_n\right)\right]\exp\left(-\frac{\Delta t}{\tau_R}\right) \tag{15}$$

$$u_{n+1} = U + \left[u_n + f\left(1-u_n\right) - U\right]\exp\left(-\frac{\Delta t}{\tau_u}\right) \tag{16}$$

Similarly, the generalized model introduced in this work can be integrated between spikes:

$$u_{n+1} = U + \left[u_n + f\left(1-u_n\right)u_n - U\right]\exp\left(-\frac{\Delta t}{\tau_u}\right) \tag{17}$$

Where $u_n^+ = u_n + f\left(1-u_n\right)u_n$ is the value of u after the spike-dependent increase following the nth spike. In both models, at time $t=0$, we assume no previous activation, therefore $R_0 = 1$ and $u_0 = U$.

Statistical Inference

To extract the properties of the model from experimental data, we developed a maximum likelihood approach. Given a set of amplitudes $\mathbf{y} = \{y_1, y_2, ..., y_i, ..., y_n\}$ resulting from a stimulation spike-train S, we want to find the parameters θ that maximize the likelihood $p(\mathbf{y}|S,\theta)$. For this, as discussed in the body of the manuscript, we used a reparameterized gamma distribution such that the shape parameter and scale parameter are written in terms of the mean, $\mu = \gamma\lambda$, and standard deviation, $\sigma = \sqrt{\gamma}\lambda$. This results in a shape parameter: $\gamma = \mu^2/\sigma^2$, and scale parameter: $\lambda = \sigma^2/\mu$. The gamma distribution is then given by:

$$g(y|\mu,\sigma) = \frac{e^{\frac{-y\mu}{\sigma^2}}\, y^{(\mu^2/\sigma^2-1)}}{\Gamma(\frac{\mu^2}{\sigma^2})\left(\frac{\sigma^2}{\mu}\right)^{\mu^2/\sigma^2}} \tag{18}$$

Thus, for the mathematical model presented here, the negative log-likelihood (NLL) is:

$$NLL(\mathbf{y}|S,\theta) = \sum_i \left[\frac{y_i\mu_i}{\sigma_i^2} - \left(\frac{\mu_i^2}{\sigma_i^2} - 1\right) \ln\left(\frac{y_i\mu_i}{\sigma_i^2}\right) + \ln\left(\frac{\Gamma(\frac{\mu_i^2}{\sigma_i^2})\sigma_i^2}{\mu_i}\right)\right] \tag{19}$$

where μ_i and σ_i are shorthand for efficacy and standard deviation at the ith spike time: $\mu_i = \mu(t_i)$, $\sigma_i = \sigma(t_i)$, that is, the elements of the vectors $\boldsymbol{\mu}$ and $\boldsymbol{\sigma}$.

We parametrized the time-dependent standard deviation and mean of the gamma distribution by expanding the filters $\mathbf{k}_\mu$ and $\mathbf{k}_\sigma$ in a linear combination of nonlinear basis: $k_\mu(t) = \sum_l a_l h_l(t)$, and $k_\sigma(t) = \sum_m c_m h_m(t)$. Typical choices for such nonlinear basis are raised cosine [32], splines [66, 67], rectangular [97] or exponential decays [34]. In counterpart to the numerical simulations where the kernels are made of a combination of exponential functions with different decay time constants, we have used this choice of basis functions.

In this framework, hyper-parameters are the choice of the number of basis functions, $l \in [0, L]$ and $m \in [0, M]$, as well as the decay timescale for each basis function $h_l(t) = \Theta(t)e^{-t/\tau_l}/\tau_l$, where $\Theta(t)$ is a Heaviside function. Free parameters are the amplitude of the basis functions $\{a_l\}$, $\{c_m\}$ and the scaling factor σ_0. By choosing hyper-parameters *a priori*, the modeller must choose a number of bases that is neither too big to cause overfitting, nor too small to cause model rigidity. The choice of time constant is made to tile exhaustively the range of physiologically relevant time scales. It is important to note that, because a combination of exponential basis functions can be used to capture a decay time scale absent from the set of τ hyper-parameters, the choice of τ does not specify the time scale of synaptic dynamics. The time-scale will be determined by inferring the relative amplitude of the basis functions. We can label the baseline parameter as the coefficient regulating the amplitude of a constant basis function, such that $a_0 = bh_0(t) = b_\mu$ and $c_0 = b_\sigma h_0(t) = b_\sigma$. There are thus $L + 1 + M + 2$ free parameters in total :

$$\theta = \{a_0, ..., a_L, \sigma_0, c_0, ..., c_M\}$$

To perform parameter inference, we first filtered the data using the set of basis functions and stored the filtered spike train just before each spike in a matrix. Each row of the matrix corresponds to an individual basis function, and each column corresponds to spike timings. The matrix, X, thus stores the result of the convolution between the various basis function (rows) and the spike train at the time of the various spikes (columns).

For simplicity, it is convenient to take the same choice of basis functions for the efficacy and the variance kernel. The amplitudes are expressed in a vector $\theta_\mu = \{a_0, ..., a_L\}$, for the efficacy kernel, and $\theta_\sigma = \{c_0, ..., c_M\}$ for the variance kernel. Using this matrix notation, the linear combination is expressed as a matrix multiplication:

$$\boldsymbol{\mu} = \frac{1}{f(a_0)} f\left(X^T \boldsymbol{\theta}_\mu\right)$$

$$\boldsymbol{\sigma} = \sigma_0 f\left(X^T \boldsymbol{\theta}_\sigma\right)$$

where $\boldsymbol{\mu}$ and $\boldsymbol{\sigma}$ have length n and can be used to evaluate the NLL according to Eq. 19 and $f(.)$ denotes the nonlinear (sigmoidal) readout. Performing a grid search of the parameter space around initialized parameter values, we can obtain the landscape for the function and ascertain the presence of convexity (see Fig. 7). The inferred parameters will then be the set of θ_μ and θ_σ minimizing the NLL over the training set.

Fitting models to surrogate and experimental data

SRP model. Minimization of the NLL across the training set was performed using a limited-memory Broyden–Fletcher–Goldfarb–Shanno algorithm with bounded parameter constrains (L-BFGS-B). For the optimization on surrogate data in Fig. 7, we chose an initial parameter estimate close to the true parameters. The resulting optimal parameter set provides an estimate of how close the NLL minimum is to the true parameter set for different numbers of training spikes. To avoid local minima when fitting the model to the experimental data in Fig. 8, we we combined the L-BFGS-B minimization algorithm with a multistart procedure. We implemented a coarse grid search across the parameter space to generate a total of 256 equally spaced starting points for the optimization algorithm and kept the parameter set that yielded the minimum NLL across all converged optimizations.

TM model. To fit the TM model to experimental data in Fig. 8, we implemented a thorough grid search across the 4-dimensional parameter space, probing 1 million parameter combinations. We kept the parameter set that minimized the mean squared error (MSE) across the training data.

Author contributions

RN conceived the study. JR, DT and RN performed the analysis. KT contributed the experimental data. JR, DT and JB generated the computational package. RN and KT supervised the project. All co-authors contributed to writing the article.

Funding

NSERC Discovery Grant 06972 (RN). CIHR Project Grant RN38364 (RN and KT). Neurasmus EMJMD scholarship (JR).

Acknowledgments

We thank Alexandre Payeur, Ezekiel Williams, Anup Pilail, Emerson Harkin and Jean-Claude Béïque for helpful comments.

References

1. Feng T. Studies on the neuromuscular junction. XXVI. The changes of the end-plate potential during and after prolonged stimulation. Chinese Journal of Physiology. 1941;16:341–372.

2. Eccles JC, Katz B, Kuffler SW. Nature of the" endplate potential" in curarized muscle. Journal of Neurophysiology. 1941;4(5):362–387.

3. Magleby K, Zengel JE. A dual effect of repetitive stimulation on post-tetanic potentiation of transmitter release at the frog neuromuscular junction. The Journal of Physiology. 1975;245(1):163–182.

4. Varela JA, Sen K, Gibson J, Fost J, Abbott L, Nelson SB. A quantitative description of short-term plasticity at excitatory synapses in layer 2/3 of rat primary visual cortex. J Neurosci. 1997;17(20):7926–7940.

5. Zucker RS, Regehr WG. Short-term synaptic plasticity. Annual review of physiology. 2002;64(1):355–405.

6. Neubrandt M, Oláh VJ, Brunner J, Marosi EL, Soltesz I, Szabadics J. Single bursts of individual granule cells functionally rearrange feedforward inhibition. Journal of Neuroscience. 2018;38(7):1711–1724.

7. Crick F. Function of the thalamic reticular complex: the searchlight hypothesis. Proc Natl Acad Sci USA. 1984;81(14):4586–4590.

8. Naud R, Sprekeler H. Sparse bursts optimize information transmission in a multiplexed neural code. Proc Nat Acad Sci (USA). 2018;doi:10.1073/pnas.1720995115.

9. Reyes A, Lujan R, Rozov A, Burnashev N, Somogyi P, Sakmann B. Target-cell-specific facilitation and depression in neocortical circuits. Nat Neurosci. 1998;1(4):279–285.

10. Scanziani M, Gähwiler BH, Charpak S. Target cell-specific modulation of transmitter release at terminals from a single axon. Proceedings of the National Academy of Sciences. 1998;95(20):12004–12009.

11. Markram H, Wu Y, Tosdyks M. Differential signaling via the same axon of neocortical pyramidal neurons. Proc Natl Acad Sci USA. 1998;95:5323–5328.

12. De Pasquale R, Sherman SM. Synaptic properties of corticocortical connections between the primary and secondary visual cortical areas in the mouse. J Neurosci. 2011;31(46):16494–16506.

13. Sherman SM. Thalamocortical interactions. Curr Opin Neurobiol. 2012;22(4):575–579.

14. Pala A, Petersen CC. In vivo measurement of cell-type-specific synaptic connectivity and synaptic transmission in layer 2/3 mouse barrel cortex. Neuron. 2015;85(1):68–75.

15. Ghanbari A, Malyshev A, Volgushev M, Stevenson IH. Estimating short-term synaptic plasticity from pre-and postsynaptic spiking. PLoS computational biology. 2017;13(9):e1005738.

16. Ghanbari A, Ren N, Keine C, Stoelzel C, Englitz B, Swadlow HA, et al. Modeling the short-term dynamics of in vivo excitatory spike transmission. Journal of Neuroscience. 2020;40(21):4185–4202.

17. Granseth B, Ahlstrand E, Lindström S. Paired pulse facilitation of corticogeniculate EPSCs in the dorsal lateral geniculate nucleus of the rat investigated in vitro. J Physiol. 2002;544(2):477–486.

18. Felmy F, Neher E, Schneggenburger R. Probing the intracellular calcium sensitivity of transmitter release during synaptic facilitation. Neuron. 2003;37(5):801–811.

19. Lefort S, Petersen CC. Layer-Dependent Short-Term Synaptic Plasticity Between Excitatory Neurons in the C2 Barrel Column of Mouse Primary Somatosensory Cortex. Cerebral Cortex. 2017;27(7):3869–3878.

20. Wang Y, Markram H, Goodman PH, Berger TK, Ma J, Goldman-Rakic PS. Heterogeneity in the pyramidal network of the medial prefrontal cortex. Nature neuroscience. 2006;9(4):534.

21. Savanthrapadian S, Meyer T, Elgueta C, Booker SA, Vida I, Bartos M. Synaptic properties of SOM-and CCK-expressing cells in dentate gyrus interneuron networks. Journal of Neuroscience. 2014;34(24):8197–8209.

22. Chamberland S, Evstratova A, Tóth K. Interplay between synchronization of multivesicular release and recruitment of additional release sites support short-term facilitation at hippocampal mossy fiber to CA3 pyramidal cells synapses. Journal of Neuroscience. 2014;34(33):11032–11047.

23. Hennig MH. Theoretical models of synaptic short term plasticity. Frontiers in computational neuroscience. 2013;7:45.

24. Tsodyks M, Markram H. The neural code between neocortical pyramidal neurons depends on neurotransmitter release probability. Proc Natl Academy of Sci, USA. 1997;94:719–723.

25. Tsodyks M, Pawelzik K, Markram H. Neural Networks with Dynamic Synapses. Neural Computation. 1998;10(4):821–835.

26. Costa RP, Sjöström PJ, Van Rossum MC. Probabilistic inference of short-term synaptic plasticity in neocortical microcircuits. Front Comput Neurosci. 2013;7.

27. Barri A, Wang Y, Hansel D, Mongillo G. Quantifying repetitive transmission at chemical synapses: a generative-model approach. eNeuro. 2016;3(2):ENEURO–0113.

28. Barroso-Flores J, Herrera-Valdez MA, Galarraga E, Bargas J. Models of Short-Term Synaptic Plasticity. In: The Plastic Brain. Springer; 2017. p. 41–57.

29. Fuhrmann G, Cowan A, Segev I, Tsodyks M, Stricker C. Multiple mechanisms govern the dynamics of depression at neocortical synapses of young rats. The Journal of physiology. 2004;557(2):415–438.

30. Chamberland S, Timofeeva Y, Evstratova A, Volynski K, Tóth K. Action potential counting at giant mossy fiber terminals gates information transfer in the hippocampus. Proceedings of the National Academy of Sciences. 2018;115(28):7434–7439.

31. Kobbersmed JR, Grasskamp AT, Jusyte M, Böhme MA, Ditlevsen S, Sørensen JB, et al. Rapid regulation of vesicle priming explains synaptic facilitation despite heterogeneous vesicle: Ca2+ channel distances. eLife. 2020;9.

32. Pillow J, Paninski L, Uzzell V, Simoncelli E, Chichilnisky E. Prediction and decoding of retinal ganglion cell responses with a probabilistic spiking model. Journal of Neuroscience. 2005;25(47):11003–11013.

33. Pillow J, Shlens J, Paninski L, Sher A, Litke A, Chichilnisky E, et al. Spatio-temporal correlations and visual signalling in a complete neuronal population. Nature. 2008;454(7207):995–999.

34. Mensi S, Naud R, Avermann M, Petersen CCH, Gerstner W. Parameter Extraction and Classification of Three Neuron Types Reveals two Different Adaptation Mechanisms. Journal of Neurophysiology. 2012;107:1756–1775.

35. Gerstner W, Kistler W, Naud R, Paninski L. Neuronal Dynamics. Cambridge: Cambridge University Press; 2014.

36. Pozzorini C, Mensi S, Hagens O, Naud R, Koch C, Gerstner W. Automated high-throughput characterization of single neurons by means of simplified spiking models. PLoS Comp Biol. 2015;11(6):e1004275.

37. Teeter C, Iyer R, Menon V, Gouwens N, Feng D, Berg J, et al. Generalized leaky integrate-and-fire models classify multiple neuron types. Nature communications. 2018;9(1):709.

38. Maass W, Zador AM. Dynamic stochastic synapses as computational units. In: Advances in neural information processing systems; 1998. p. 194–200.

39. Oswald AMM, Lewis JE, Maler L. Dynamically interacting processes underlie synaptic plasticity in a feedback pathway. Journal of neurophysiology. 2002;87(5):2450–2463.

40. Chichilnisky EJ. A simple white noise analysis of neuronal light responses. Network. 2001;12(2):199–213.

41. Paninski L. Maximum likelihood estimation of cascade point-process neural encoding models. Network: Computation in Neural Systems. 2004;15:243–262.

42. Truccolo W, Eden U, Fellows M, Donoghue JP, Brown EN. A point process framework for relating neural spiking activity to spiking history, neural spiking activity to spiking history, neural ensemble, and extrinsic covariate effects. Journal of Neurophysiology. 2005;93:1074–1089.

43. Wu MCK, David SV, Gallant JL. Complete functional characterization of sensory neurons by system identification. Annu Rev Neurosci. 2006;29:477–505.

44. Ostojic S, Brunel N. From spiking neuron models to linear-nonlinear models. PLoS Comput Biol. 2011;7(1):e1001056. doi:10.1371/journal.pcbi.1001056.

45. McFarland JM, Cui Y, Butts DA. Inferring nonlinear neuronal computation based on physiologically plausible inputs. PLoS computational biology. 2013;9(7):e1003143.

46. Vintch B, Movshon JA, Simoncelli EP. A convolutional subunit model for neuronal responses in macaque V1. Journal of Neuroscience. 2015;35(44):14829–14841.

47. Ujfalussy BB, Makara JK, Lengyel M, Branco T. Global and Multiplexed Dendritic Computations under In Vivo-like Conditions. Neuron. 2018;100(3):579–592.

48. Gerstner W, van Hemmen JL. Associative memory in a network of 'spiking' neurons. Network. 1992;3:139–164.

49. Jolivet R, Rauch A, Lüscher H, Gerstner W. Predicting spike timing of neocortical pyramidal neurons by simple threshold models. Journal of Computational Neuroscience. 2006;21:35–49.

50. Markram H, Wang Y, Tsodyks M. Differential signaling via the same axon of neocortical pyramidal neurons. Proc Natl Acad Sci USA. 1998;95(9):5323–5328.

51. Vyleta NP, Jonas P. Loose coupling between Ca2+ channels and release sensors at a plastic hippocampal synapse. Science. 2014;343(6171):665–670.

52. Scott R, Rusakov DA. Main determinants of presynaptic Ca2+ dynamics at individual mossy fiber–CA3 pyramidal cell synapses. Journal of Neuroscience. 2006;26(26):7071–7081.

53. Fuhrmann G, Segev I, Markram H, Tsodyks M. Coding of temporal information by activity-dependent synapses. Journal of neurophysiology. 2002;87(1):140–148.

54. Loebel A, Le Bé JV, Richardson MJ, Markram H, Herz AV. Matched pre-and post-synaptic changes underlie synaptic plasticity over long time scales. Journal of Neuroscience. 2013;33(15):6257–6266.

55. He L, Wu LG. The debate on the kiss-and-run fusion at synapses. Trends in neurosciences. 2007;30(9):447–455.

56. Soares C, Trotter D, Longtin A, Béïque JC, Naud R. Parsing out the variability of transmission at central synapses using optical quantal analysis. bioRxiv. 2019; p. 624692.

57. Bekkers J, Richerson G, Stevens C. Origin of variability in quantal size in cultured hippocampal neurons and hippocampal slices. Proceedings of the National Academy of Sciences. 1990;87(14):5359–5362.

58. Larkman A, Hannay T, Stratford K, Jack J. Presynaptic release probability influences the locus of long-term potentiation. Nature. 1992;360(6399):70.

59. Lavoie N, Jeyaraju DV, Peralta MR, Seress L, Pellegrini L, Tóth K. Vesicular zinc regulates the Ca2+ sensitivity of a subpopulation of presynaptic vesicles at hippocampal mossy fiber terminals. Journal of Neuroscience. 2011;31(50):18251–18265.

60. Bhumbra GS, Beato M. Reliable evaluation of the quantal determinants of synaptic efficacy using Bayesian analysis. Journal of neurophysiology. 2013;109(2):603–620.

61. Hefft S, Kraushaar U, RP Geiger J, Jonas P. Presynaptic short-term depression is maintained during regulation of transmitter release at a GABAergic synapse in rat hippocampus. The Journal of physiology. 2002;539(1):201–208.

62. Gerstner W, Naud R. How Good Are Neuron Models? Science. 2009;326:379–380.

63. Dobrunz LE, Stevens CF. Response of hippocampal synapses to natural stimulation patterns. Neuron. 1999;22(1):157–166.

64. Richards BA, Lillicrap TP. Dendritic solutions to the credit assignment problem. Curr Opin Neurobiol. 2019;54:28–36.

65. Advani MS, Saxe AM, Sompolinsky H. High-dimensional dynamics of generalization error in neural networks. Neural Networks. 2020;132:428–446.

66. Kass RE, Ventura V. A spike-train probability model. Neural Computation. 2001;13:1713–1720.

67. Gerhard F, Pipa G, Lima B, Neuenschwander S, Gerstner W. Extraction of network topology from multi-electrode recordings: is there a small-world effect? Frontiers in computational neuroscience. 2011;5:4.

68. McCullagh P, Nelder JA. Generalized linear models. vol. 37. 2nd ed. Chapman & Hall/CRC; 1998.

69. Zhao M, Iyengar S. Nonconvergence in logistic and poisson models for neural spiking. Neural computation. 2010;22(5):1231–1244.

70. Stevenson IH. Omitted variable bias in GLMs of neural spiking activity. Neural computation. 2018;30(12):3227–3258.

71. Srivastava N, Hinton G, Krizhevsky A, Sutskever I, Salakhutdinov R. Dropout: a simple way to prevent neural networks from overfitting. The journal of machine learning research. 2014;15(1):1929–1958.

72. LeCun Y, Kavukcuoglu K, Farabet C. Convolutional networks and applications in vision. In: Proceedings of 2010 IEEE international symposium on circuits and systems. IEEE; 2010. p. 253–256.

73. Dahl GE, Sainath TN, Hinton GE. Improving deep neural networks for LVCSR using rectified linear units and dropout. In: 2013 IEEE international conference on acoustics, speech and signal processing. IEEE; 2013. p. 8609–8613.

74. Zeghidour N, Xu Q, Liptchinsky V, Usunier N, Synnaeve G, Collobert R. Fully convolutional speech recognition. arXiv preprint arXiv:181206864. 2018;.

75. Payeur A, Béïque JC, Naud R. Classes of dendritic information processing. Current opinion in neurobiology. 2019;58:78–85.

76. Pillow JW, Paninski L, Simoncelli EP. Maximum Likelihood estimation of a stochastic integrate-and-fire model. In: Thrun S, Saul L, Schölkopf B, editors. Advances in Neural Information Processing Systems. vol. 16; 2004. p. 1311–1318.

77. Schröder C, James B, Lagnado L, Berens P. Approximate bayesian inference for a mechanistic model of vesicle release at a ribbon synapse. In: Advances in Neural Information Processing Systems; 2019. p. 7068–7078.

78. Lee JH, Campagnola L, Seeman SC, Jarsky TH, Mihalas SH. Functional synapse types via characterization of short-term synaptic plasticity. bioRxiv. 2019; p. 648725.

79. Ghanbari A, Ren N, Keine C, Stoelzel C, Englitz B, Swadlow H, et al. Functional connectivity with short-term dynamics explains diverse patterns of excitatory spike transmission in vivo. bioRxiv. 2018; p. 475178.

80. Aitchison L, Pouget A, Latham PE. Probabilistic synapses. arXiv preprint arXiv:14101029. 2014;.

81. Schmutz V, Gerstner W, Schwalger T. Mesoscopic population equations for spiking neural networks with synaptic short-term plasticity. The Journal of Mathematical Neuroscience. 2020;10(1):1–32.

82. Grillo FW, Neves G, Walker A, Vizcay-Barrena G, Fleck RA, Branco T, et al. A distance-dependent distribution of presynaptic boutons tunes frequency-dependent dendritic integration. Neuron. 2018;99(2):275–282.

83. Barros Zulaica N, Rahmon J, Chindemi G, Perin R, Markram H, Ramaswamy S, et al. Estimating the Readily-Releasable Vesicle Pool Size at Synaptic Connections in a Neocortical Microcircuit. Frontiers in synaptic neuroscience. 2019;11:29.

84. Larkum M, Nevian T, Sandler M, Polsky A, Schiller J. Synaptic integration in tuft dendrites of layer 5 pyramidal neurons: a new unifying principle. Science. 2009;.

85. Kayser C, Montemurro M, Logothetis N, Panzeri S. Spike-phase coding boosts and stabilizes information carried by spatial and temporal spike patterns. Neuron. 2009;61(4):597–608.

86. Herzfeld DJ, Kojima Y, Soetedjo R, Shadmehr R. Encoding of action by the Purkinje cells of the cerebellum. Nature. 2015;526(7573):439.

87. Lecun Y, Bengio Y. Convolutional networks for images, speech, and time-series. In: The handbook of brain theory and neural networks. MIT Press; 1995.

88. Krizhevsky A, Sutskever I, Hinton GE. Imagenet classification with deep convolutional neural networks. In: Advances in neural information processing systems; 2012. p. 1097–1105.

89. Sylwestrak EL, Ghosh A. Elfn1 regulates target-specific release probability at CA1-interneuron synapses. Science. 2012;338(6106):536–540.

90. Senn W, Tsodyks M, Markram H. An algorithm for modifying neurotransmitter release probability based on pre- and postsynaptic spike timing. Neural Computation. 2001;13:35–67.

91. Costa RP, Padamsey Z, D'Amour JA, Emptage NJ, Froemke RC, Vogels TP. Synaptic transmission optimization predicts expression loci of long-term plasticity. Neuron. 2017;96(1):177–189.

92. Sjöström PJ, Turrigiano GG, Nelson SB. Multiple forms of long-term plasticity at unitary neocortical layer 5 synapses. Neuropharmacology. 2007;52(1):176–184.

93. Ding S, Li L, Zhou FM. Presynaptic serotonergic gating of the subthalamonigral glutamatergic projection. Journal of Neuroscience. 2013;33(11):4875–4885.

94. Takkala P, Woodin MA. Muscarinic acetylcholine receptor activation prevents disinhibition-mediated LTP in the hippocampus. Frontiers in cellular neuroscience. 2013;7:16.

95. Payeur A, Guerguiev J, Zenke F, Richards BA, Naud R. Burst-dependent synaptic plasticity can coordinate learning in hierarchical circuits. bioRxiv. 2020;doi:10.1101/2020.03.30.015511.

96. Keijser J, Sprekeler H. Interneuron diversity is required for compartment-specific feedback inhibition. bioRxiv. 2020;.

97. Pozzorini C, Naud R, Mensi S, Gerstner W. Temporal whitening by power-law adaptation in neocortical neurons. Nat Neurosci. 2013;16(7):942–948.